

Effect of substitutions and defects in half-Heusler FeVSb studied by electron transport measurements and KKR-CPA electronic structure calculations

L. Jodin, J. Tobola,* P. Pecheur, and H. Scherrer

Laboratoire de Physique des Matériaux, Ecole des Mines INPL, Parc du Saurupt, 54042 Nancy Cedex, France

S. Kaprzyk

Faculty of Physics and Nuclear Techniques, AGH University of Science and Technology, Al. Mickiewicza 30, 30-059 Cracow, Poland

(Received 9 June 2004; published 18 November 2004)

The structural and electron transport properties of the pure and Co-, Ti-, and Zr-substituted FeVSb half-Heusler phases have been investigated using x-ray diffraction, Mössbauer spectroscopy, and Electron Probe Microscopy Analysis as well as resistivity, thermopower, and Hall effect measurements in the 80–900 K temperature range. In a parallel study, the electronic structures of FeVSb and the aforementioned alloys were calculated using the Korringa-Kohn-Rostoker method with the coherent potential approximation (KKR-CPA) in the LDA framework. The electronic densities of states and dispersion curves were obtained. The crystal structure stability and site preference analysis were addressed using total energy computations. Most of these experimental results correspond to electronic structure computations only if they take into account extra crystal defects such as antisite defects or vacancies present to various extents in the samples. Indeed a remarkable variation of KKR-CPA density of states occurring both in FeVSb and $\text{FeV}_{1-x}\text{Zr}_x\text{Sb}$ including defects may explain why FeVSb is not fully semiconducting as well as why there is a change of the thermopower sign in the $\text{FeV}_{1-x}\text{Zr}_x\text{Sb}$ versus x content.

DOI: 10.1103/PhysRevB.70.184207

PACS number(s): 61.10.-i, 61.18.Fs, 71.20.-b, 71.23.-k

I. INTRODUCTION

Half-Heusler phases are particularly appealing systems since a wide spectrum of complex physical properties appears in a relatively simple C1_b structure. Many studies on magnetic, transport, and electronic structure properties have revealed that semiconductors, semimetals, Pauli metals, ferromagnets, half-metallic ferromagnets, or antiferromagnets can exist in this series of compounds.^{1–3} On the whole, it has also been noticed that such a variety of behaviors may come from the presence of an energy gap in the density of states for the valence electron count $\text{VEC}=18$.^{4,5} The semiconducting properties in the half-Heusler compounds were first deduced from the resistivity and optical measurements in NiMSn ($M=\text{Ti, Zr, Hf}$)^{6,7} and later supported by band structure computations.^{8–10} Further theoretical works^{4,11–14} have often disclosed that in various $\text{VEC}=18$ compounds an energy gap appears above the 9th band in a quite systematic way. The gap varies from 0.3 eV (NiYSb) to 1.2 eV (CoZrSb) in the LDA results. So, the transport and magnetic properties of compounds (with $\text{VEC} \neq 18$) strongly depend on the Fermi level position with respect to this gap. However, such a simple picture may be modified if different kinds of atomic disorder (vacancies, antisite defects) arise.^{8,15,16} Further experimental works have presented new half-Heusler systems,^{17–19} in which most of the $\text{VEC}=18$ compounds exhibit semiconducting-like (or semimetallic-like) and Pauli paramagnetic behaviors. Special attention was paid to investigations of remarkable thermoelectric properties, e.g., in NiMSn ($M=\text{Ti, Zr, Hf}$)^{20,21} and CoMSb ($M=\text{Ti, Zr, Hf}$)^{22,23} upon doping with transition metal elements. All these findings open apparently new perspectives for selected half-Heusler materials as efficient thermoelectrics.^{24,25} In the

aforementioned context the electron transport characteristics were also investigated in other C1_b phases such as FeVSb ^{26,27} and NiRESb ($RE=\text{Tb, Dy, Ho}$).²⁸ Moreover, a metal-semiconductor-metal crossover with some unusual thermopower variation versus composition has been recently detected in $\text{Fe}_{1-x}\text{Ni}_x\text{TiSb}$ ²⁹ and other solid solutions,³⁰ which gives additional experimental evidence for the $\text{VEC}=18$ band gap “rule” in disordered half-Heusler samples.

The half-Heusler XYZ phases are ternary compounds with equal composition 1:1:1, where X represents a transition metal element, Y is either a transition metal, rare earth or noble element, whereas Z denotes a sp element such as Sn, Sb, or Bi. These compounds crystallize in the face centered cubic (fcc) structure (space group $F-43m$, AgMgAs -type) as shown in Fig. 1. Thus one unit cell holds four formula units with the X , Y , and Z atoms located in the $4a:(0,0,0)$, $4d:(\frac{3}{4}, \frac{3}{4}, \frac{3}{4})$ and $4c:(\frac{1}{4}, \frac{1}{4}, \frac{1}{4})$ positions, respectively. The ori-

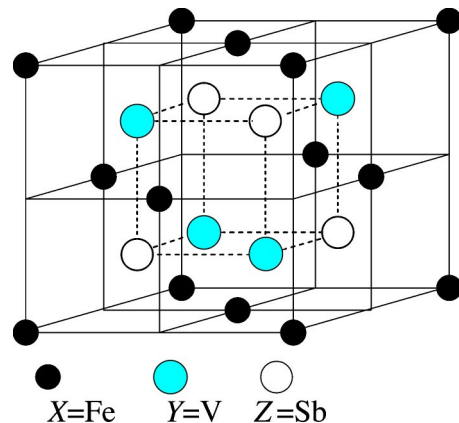


FIG. 1. Crystal structure of half-Heusler FeVSb.

gin of the unit cell is sometimes specified on the Y atom.³¹ The $C1_b$ structure (Fig. 1) consists of four interpenetrating fcc sublattices equally displaced along a body diagonal of the unit cell, if accounting for a vacancy at $4b: (\frac{1}{2}, \frac{1}{2}, \frac{1}{2})$. This structure can also be described as a rock-salt structure built of Y and Z atoms, in which a half of the tetrahedral sites is occupied by X atoms in an ordered way. When filling up remaining voids with additional X atoms, we obtain the $L2_1$ structure (space group $Fm\bar{3}m$, Cu_2MnAl -type) which is characteristic of the normal Heusler X_2YZ phases. Some of the $C1_b$ compounds, like $FeVSb$ or $NiVSb$, may also crystallize in a hexagonal structure (space group $P6_3/mmc$, Ni_2In -type) under high temperature.¹⁷

In this work we present structural and electrical transport properties of pure and doped $FeVSb$ studied using x-ray diffraction, Mössbauer spectroscopy, and Electron Probe Microanalysis (EPMA) as well as resistivity and thermopower measurements. The substituted elements were Co (as n type) and Ti , Zr (as p type). Furthermore, we report the electronic structure of these systems based on the Korringa-Kohn-Rostoker (KKR) calculations with the coherent potential approximation (CPA). A total energy analysis was also undertaken to obtain insight into the structural stability of ordered $FeVSb$ and the site preference of substituted elements. The electronic structure calculations were used for a qualitative interpretation of experimental results.

The paper is organized as follows. In Sec. II we briefly describe the sample preparation and the structural data analysis. In Sec. III we present the results for pure $FeVSb$. First, the band structure calculations are shown, then experimental results of electron transport measurements such as the resistivity $\rho(T)$ and thermopower $S(T)$ are described. These are discussed in the light of the band structure calculations, accounting for various native defects in the crystal. In Sec. IV we report the electronic structure and experimental results for doped $FeVSb$ and related systems, also accounting for the aforementioned native defects. In Sec. V we summarize this work, paying attention to the possible origins of agreements and discrepancies between theory and experiments.

II. SAMPLE PREPARATION AND STRUCTURAL ANALYSIS

Polycrystalline samples were prepared in an induction furnace. High purity elements were melted in a cold water cooled copper crucible under argon atmosphere. After melting the metals, antimony was added with a slight excess to compensate for evaporation. The resulting compounds contained fcc and hcp phases. A differential thermal analysis was performed to determine the cubic-hexagonal phase transition temperature in $FeVSb$, which is near $700^\circ C$. The samples wrapped in molybdenum foil were annealed under helium-hydrogen at $650^\circ C$ for one week. The composition and structure of the compounds were investigated by x-ray diffraction measurement and EPMA analysis. The cell parameters were established via a powder x-ray diffraction pattern (Fig. 2) using high purity silicon as an internal standard.

Table I gives the room temperature lattice parameters of pure and substituted (with Ti , Zr , and Co) $FeVSb$. The cubic

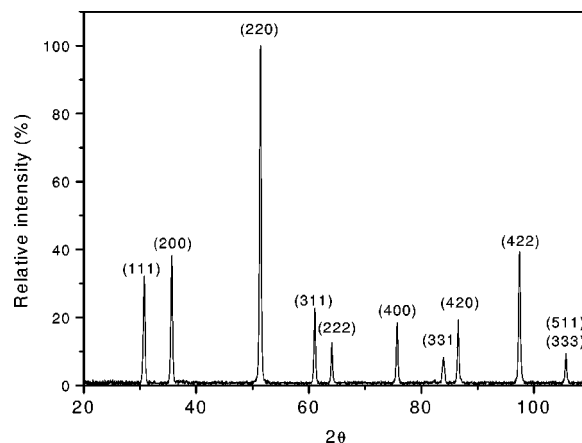


FIG. 2. X-ray diffraction pattern in $FeVSb$.

($AgMgAs$ -type) and hexagonal (Ni_2In -type) structures were observed in all investigated samples. The lattice constants of both structural variants of $FeVSb$ were found to be in perfect agreement with the previously reported values.³¹ From a comparison with experimental data obtained in the alloys one concludes that the lattice constant in $Fe_{1-x}Co_xVSb$ does not change at least for a small Co amount. Conversely, a significant enhancement of lattice parameters was detected in $FeV_{1-x}Ti_xSb$ when the Ti concentration increases in the cubic structure (also in the hexagonal structure), which is probably due to quite different atomic radii of Ti and V . The variation of the lattice constant in the cubic structure (for $0 < x < 0.2$) follows more or less a straight line versus the Ti content and is also close to values fitted to Vegard's law between $FeVSb$ ($a = 5.826 \text{ \AA}$) and $FeTiSb$ ($a = 5.951 \text{ \AA}$).

Electron Probe Microanalyses were performed strictly at the same working conditions in the investigated specimens and enabled us to determine the relative proportions among the different atoms with a standard accuracy of order of 1%. On the whole we found that all annealed samples contained various extents of an excess of antimony. Most of them also

TABLE I. Cell parameters of the cubic phase ($AgMgAs$ -type) and hexagonal phase (Ni_2In -type) for investigated half-Heusler samples.

Composition	Lattice parameters (\AA)		
	Cubic	Hexagonal	
$FeVSb$	5.826(1)	$a = 4.229(4)$	$c = 5.443(1)$
$Fe_{0.98}Co_{0.02}VSb$	5.826(0)	$a = 4.224(8)$	$c = 5.451(9)$
$FeV_{0.95}Ti_{0.05}Sb$	5.833(5)	$a = 4.225(1)$	$c = 5.468(2)$
$FeV_{0.90}Ti_{0.10}Sb$	5.842(6)	$a = 4.219(8)$	$c = 5.502(2)$
$FeV_{0.85}Ti_{0.15}Sb$	5.852(1)	$a = 4.202(2)$	$c = 5.537(2)$
$FeV_{0.80}Ti_{0.20}Sb$	5.856(9)	$a = 4.198(6)$	$c = 5.543(8)$
$FeV_{0.90}Zr_{0.10}Sb$	5.830(8)		
$FeV_{0.85}Zr_{0.15}Sb$	5.869(7)		

TABLE II. Nominal and Electron Probe Microanalysis (EPMA) composition of half-Heusler phases.

Nominal	EMPA
FeVSb	Fe _{0.98} V _{0.99} Sb _{1.03}
Fe _{0.995} Co _{0.005} VSb	Fe _{0.97} Co _{0.006} V _{0.99} Sb _{1.03}
Fe _{0.98} Co _{0.02} VSb	Fe _{0.95} Co _{0.02} V _{1.02} Sb _{1.01}
FeV _{0.90} Ti _{0.10} Sb	Fe _{0.96} V _{0.9} Ti _{0.1} Sb _{1.04}
FeV _{0.85} Ti _{0.15} Sb	Fe _{0.98} V _{0.86} Ti _{0.15} Sb _{1.01}
FeV _{0.80} Ti _{0.20} Sb	Fe _{0.99} V _{0.77} Ti _{0.22} Sb _{1.02}
FeV _{0.95} Zr _{0.05} Sb	Fe _{0.95} V _{0.98} Zr _{0.02} Sb _{1.05}
FeV _{0.90} Zr _{0.10} Sb	Fe _{0.96} V _{0.97} Zr _{0.03} Sb _{1.04}
FeV _{0.85} Zr _{0.15} Sb	Fe _{0.95} V _{0.93} Zr _{0.07} Sb _{1.05}

displayed a deficiency of iron. The relative proportions of the atoms in the investigated samples as derived from the EPMA analysis are listed in Table II. Interestingly, a comparison of obtained data for the isoelectronic series of compounds, FeV_{1-x}Zr_xSb and FeV_{1-x}Ti_xSb, indicated that the nonstoichiometry is more pronounced in the Zr-containing samples with respect to the Ti-containing ones. Further attempts to prepare stoichiometric samples by melting elements within the exact proportions led to similar results and the compounds always exhibited an excess of antimony and a deficiency of iron.

⁵⁷Fe Mössbauer spectroscopy measurements were performed to study a possible disorder in FeVSb. An iron spectrum was collected at room temperature using a standard constant-acceleration spectrometer with the 25 mCi source of ⁵⁷Co in a rhodium matrix. The obtained Mössbauer spectrum (Fig. 3) can be analyzed with a singlet (single peak), indicating that Fe atoms occupy exclusively one site. Note that irons on X and vacancy sites possess an identical atomic neighborhood and the two positions cannot be distinguished within this technique. Moreover, both ordered FeVSb and VFeSb crystallographic variants of the system are expected to result in a singlet from the ⁵⁷Fe Mössbauer spectroscopy due to the same point symmetry of both sites. Nevertheless, recent neutron diffraction spectroscopy measurements³² excluded the VFeSb possibility. Table III gives a comparison of

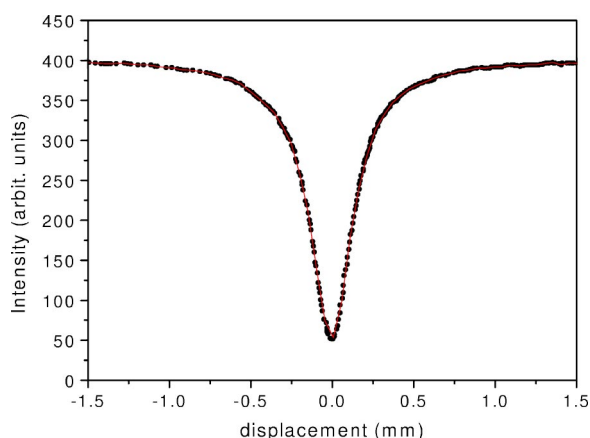


FIG. 3. Mössbauer spectrum in FeVSb.

TABLE III. Observed and calculated intensity ratio in FeVSb (calculated x-ray intensities correspond to a disorder as large as 5%).

Disorder type	I ₁₁₁ /I ₂₂₀	I ₂₀₀ /I ₂₂₀
Experimental	0.39	0.43
Ordered	0.44	0.44
Fe on V site	0.44	0.44
Fe on Sb site	0.43	0.39
Fe on a vacancy site	0.41	0.44
V/Sb exchange	0.39	0.44
V/Sb exchange ^a	0.39	0.40

^a5% Sb excess on Fe site in addition.

observed x-ray diffraction intensity ratios with values calculated using Fullprof program³³ for the perfectly ordered sample as well as accounting for different types of disorder (as large as 5%).²⁹ The detected atomic disorder may arise from the V/Sb exchange and should not be larger than 5%. Additionally, an introduced excess of Sb on the Fe site (as large as 5%) decreased only the I₂₀₀/I₂₂₀ peak ratio.

III. FeVSb

A. Computational details

The band structure of an ordered FeVSb compound for two allotropic forms (cubic and hexagonal) was determined using self-consistent Korringa-Kohn-Rostoker (KKR) calculations within the local density approximation (LDA). The electronic structure of FeVSb, containing native crystal defects (such as vacancies or antistructure defects), was also investigated within the coherent potential approximation (CPA) in KKR-CPA calculations. Since the KKR and KKR-CPA codes are different, it was verified by our computations of the limiting case of vanishing defects concentration, that both gave similar results. Moreover, KKR total energy computations were performed to determine the ground state of crystallographic variants admitted in the half-Heusler C1_b structure (FeVSb, VSbFe, and SbFeV).

In the XYZ half-Heusler structure, X, Y, and Z atoms are on (0,0,0), ($\frac{3}{4}, \frac{3}{4}, \frac{3}{4}$), and ($\frac{1}{4}, \frac{1}{4}, \frac{1}{4}$) sites, respectively. So, atomic occupancy in the FeVSb (X=Fe, Y=V, and Z=Sb) and other crystallographic variants (VSbFe and SbFeV) can be easily detected. The vacancy placed on the ($\frac{1}{2}, \frac{1}{2}, \frac{1}{2}$) site was represented by an empty sphere with no nuclear charge (Z=0). This geometrical modification permitted us to increase filling of the Wigner-Seitz cell by the nonoverlapping spheres up to 68%, if equal radii were chosen for all atoms and a vacancy. Such computational geometry enabled us to perform an accurate comparison of local electronic properties for the same atoms placed in different atomic surroundings.

In the hexagonal structure of FeVSb (Ni₂In-type) Fe, V, and Sb occupy 2a:(0,0,0), 2c:($\frac{1}{3}, \frac{2}{3}, \frac{1}{4}$) and 2d:($\frac{1}{3}, \frac{2}{3}, \frac{3}{4}$) sites, respectively. Moreover, the electronic structure of other crystallographic variants SbFeV and VSbFe in the hexagonal

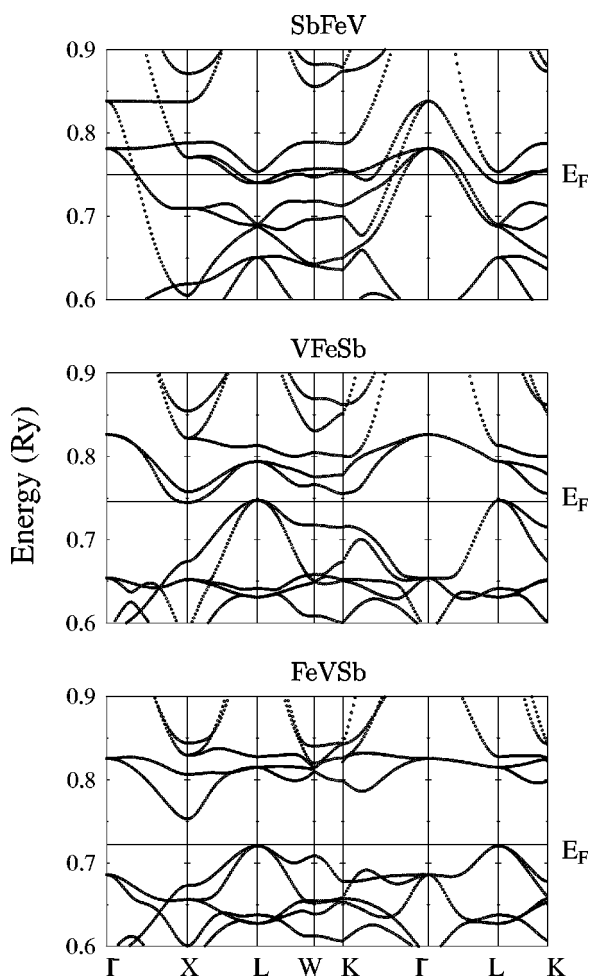


FIG. 4. KKR dispersion curves in FeVSb (semiconductor), VFeSb (semimetal), and SbFeV (metal) in the $C1_b$ structure (see the text).

structure were also considered. All computations employed the experimental values of the lattice constants (Table I). The crystal potential of the muffin-tin form was constructed within the local density approximation (LDA), using the von Barth-Hedin formula for the exchange-correlation part.³⁴ The Fermi level was determined directly from the generalized Lloyd formula.³⁵ The self-consistency cycles were repeated until input-output potentials and charges inside muffin-tin spheres were less than 1 mRy and 0.001 electron, respectively. For the final potential, the total density of states (DOS), site-decomposed DOS and l -decomposed DOS (with $l_{\max}=2$) were computed using the tetrahedron \mathbf{k} -space integration technique. The dispersion curves $E(\mathbf{k})$ were computed along high symmetry directions in the irreducible part of the Brillouin zone. More details concerning the KKR and KKR-CPA methodology used in our computations can be found in the papers.^{36–39}

B. Electronic structure of pure FeVSb

From the previous theoretical studies we know that the half-Heusler FeVSb with the $C1_b$ structure belongs to narrow band semiconductors, which is often the case in the VEC

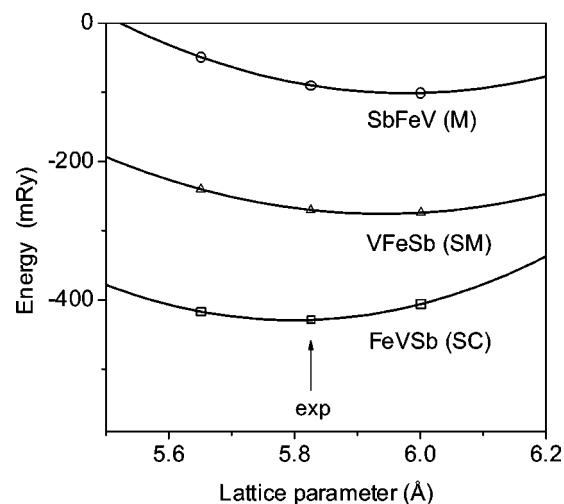


FIG. 5. Total energy versus lattice constant in FeVSb (semiconductor), VFeSb (semimetal), and SbFeV (metal).

=18 compounds. The LDA energy gap (E_g) is as large as 0.46 eV and arises between the L point at the top of the valence band and the X point at the bottom of the conduction band (Fig. 4). The KKR result is close to the E_g value obtained from the localized spherical wave method,⁴⁰ LMTO²⁷ and recently from the FP-LMTO⁴¹ computations. As the half-Heusler structure is far from compact, it may be subject to lattice instabilities. It was observed experimentally that physical properties of these compounds strongly depend on synthesis conditions and especially on thermal treatment.

In the half-Heusler unit cell, only three nonequivalent atomic arrangements are possible: FeVSb, SbFeV, and VFeSb. These three atomic arrangements have completely different ground states, i.e., FeVSb is a semiconductor, VFeSb a semimetal, while SbVFe is a metal (computed at the experimental lattice constant). Figure 4 shows the dispersion curves in the vicinity of the Fermi level in these three variants. We notice that in VFeSb the valence and conduction bands exactly touch the Fermi level (at different \mathbf{k} points) indicating a pseudo-gap behavior (we recall that a similar electronic structure was found in the normal Heusler Fe_2VAl and Fe_2VGa ^{39,46}), whereas in SbVFe E_F apparently crosses the bands along most of the BZ directions, resulting in a finite density of states like in metals. The analysis of electronic properties for various atomic arrangements were already investigated in other $C1_b$ compounds with the LMTO computations.¹⁰

Highly accurate calculations of the three aforementioned cases revealed that the FeVSb configuration, which results in a semiconducting ground state, was energetically much favored with respect to the other crystallographic variants (Fig. 5). Using the experimental lattice constant the total energy of FeVSb was found to be about 2.1 eV and 4.3 eV lower than the values computed in SbFeV and VFeSb, respectively. The KKR preference of the FeVSb phase remains in fair agreement with the recent FP-LMTO study.⁴¹ Furthermore, the FLAPW calculations⁴⁵ of $\text{Ni}(\text{Ti}, \text{Zr}, \text{Hf})\text{Sn}$ and $\text{Ni}(\text{Sc}, \text{Y}, \text{La})\text{Sb}$ have revealed evidently that the lowest energy atomic configuration corresponds to the semiconducting state.

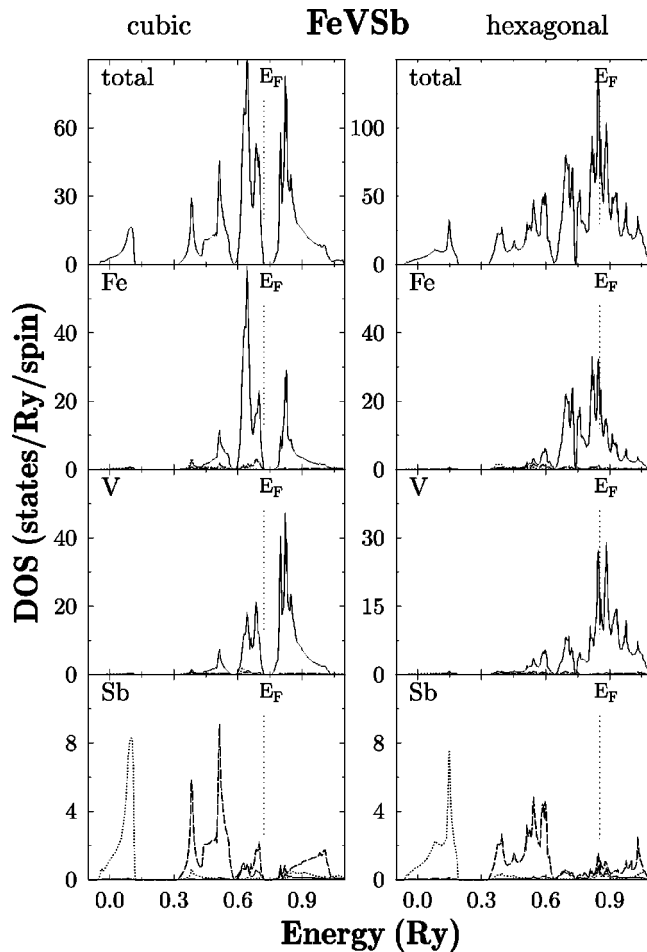


FIG. 6. Total and partial DOS on Fe, V, and Sb sites in cubic and hexagonal phases of FeVSb. In the site-decomposed DOS s , p , and d contributions are plotted by dotted, dashed, and full lines, respectively.

Figure 6 presents the total and site and l -decomposed DOS in the lowest energy FeVSb compound. The band gap in this system arises mainly from a strong hybridization of the d states of the transition metal atoms (Fe mostly below the gap, V mostly above the gap). The s and p states of Sb add 8 states to the valence bands.^{14,41,42} According to the previous and present KKR electronic structure computations the stability of the VEC=18 compounds seems to be due to the presence of the energy gap at the Fermi level. In Fig. 6 we also show the electronic structure of the high temperature hexagonal phase of FeVSb. In contrast to the cubic phase, it exhibits a continuous energy spectrum of DOS with a rather high DOS value at the Fermi level attributed to large peaks of d states detected on transition metal sites. As the DOS values at E_F satisfy the Stoner limit both on Fe and V, then it is not surprising that the spin-polarized KKR computations result in magnetic moments both on iron ($1.9 \mu_B$) and vanadium ($0.9 \mu_B$). However, arranging atoms in a different manner in the hexagonal structure may lead to a nonmagnetic ground state (due to low DOS at E_F).

A comparison of the electronic structures occurring for various atomic arrangements in the half-Heusler structure gives only an approximate insight into electronic phenomena

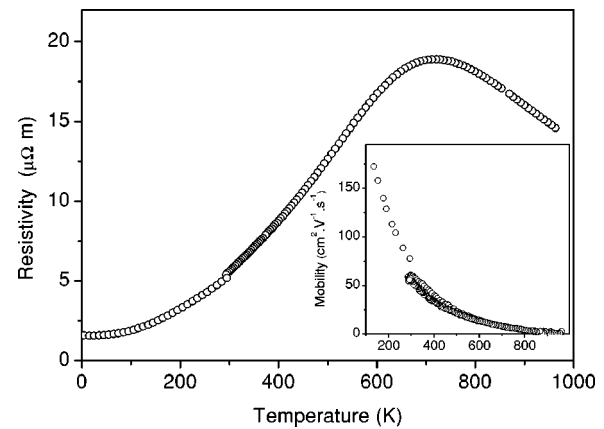


FIG. 7. Temperature dependence of the electrical resistivity and mobility (inset) in FeVSb.

that may occur in real samples, since the experimentally detected disorder in the cubic FeVSb is not larger than a few percent. Hence, intermediate cases should be investigated theoretically for a better understanding (see Sec. III D where KKR-CPA was used).

C. Electronic transport measurements

Electrical resistivities have been measured using the van der Pauw method.⁴³ Samples were prepared as square pieces of approximately 4×4 mm with a thickness smaller than 1 mm by cutting with a diamond wire. The measurement system allowed performing experiments in two temperature regimes, either at low (80–350 K) or at high (300–800 K) temperatures. In the Hall experiments the magnetic field was reversed and the Hall resistivity was obtained as $R_H = [\rho(H) - \rho(-H)]/2$. Then the carrier concentration was deduced from the relation $n = (R_H e)^{-1}$ considering that only one type of carrier was present. This should be valid due to the presence of defects (see the next section) and a transition to intrinsic behavior only above 650 K as seen in the resistivity measurements. Contacts to samples were made with silver epoxy paint at low temperatures, while molybdenum rods were applied at high temperatures. The measurements of the

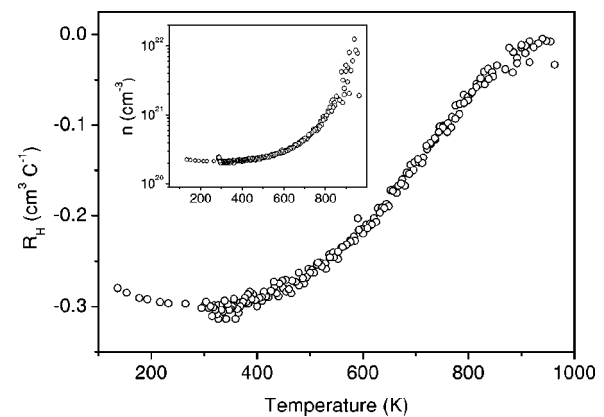


FIG. 8. Temperature dependence of the Hall constant and the carrier concentration in FeVSb.

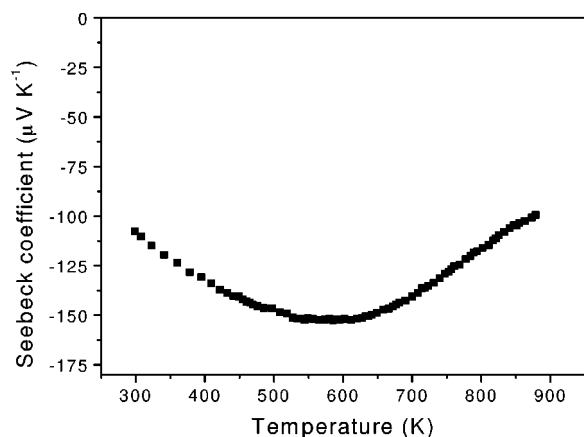


FIG. 9. Temperature dependence of the Seebeck coefficient in FeVSb.

thermopower were done using a standard differential method.⁴⁴

The temperature dependence of the electrical resistivity from 4 to 950 K is shown in Fig. 7. It exhibits two types of behavior: from 4 to 650 K, the resistivity curve increases with temperature as in a metal and above 650 K it decreases with temperature as in a semiconductor. The Hall resistivity is negative (Fig. 8).

The mobility decreases when the temperature increases and becomes very low at high temperature (Fig. 7). The carrier concentration is rather constant, near 10^{20} cm^{-3} and increases only for the temperature range above 550 K (Fig. 8). The negative Seebeck coefficient presents a minimum at about 600 K and then increases (Fig. 9).

All these results exhibit two types of behavior versus temperature: a metallic behavior below about 650 K, and a semi-conducting one above 650 K. This change of behavior seems to be best interpreted as a transition between a highly doped saturation regime and an intrinsic regime above 650 K. The corresponding gap value can be determined at high temperature using the activation law $\rho = \rho_0 \exp(-E_g/2k_B T)$ where E_g is the energy gap value and k_B is the Boltzmann constant. The obtained value for E_g is about 0.19 eV.

D. Electronic structure of FeVSb with defects

The transport properties exhibit a rather metallic behavior at low temperature while the band structure calculations predict a semiconductor. Moreover, the calculated gap is about 0.46 eV but the experimental gap is about 0.19 eV. The known deficiencies of the LDA approximation (but these usually lead to an underestimation of the band gap width) and point defects are a possible explanation for these differences. We first investigated the effect of the site disorder of V and Sb on the band structure. From the KKR-CPA computations, we obtained upon the inclusion of V/Sb and Fe/V antisite defects (conserving a 1:1:1 stoichiometry among Fe, V, and Sb) the Fermi level still located in the gap, with the width of E_g progressively reduced when the number of intermixing atoms increased.¹⁶ This effect was earlier detected in pseudopotential computations for Ni(Ti, Zr, Hf)Sn⁸

where the Zr/Sn disorder practically closed the energy gap at 15% of the exchanged atoms. This type of disorder reduces the gap but the Fermi level remains inside the gap. The calculation can explain the low value of the experimental gap, but not the metallic behavior observed below 650 K.

From the above-mentioned EMPA analysis of several FeVSb samples (Table II), with a deficiency of iron, we expect that some excess Sb or Fe vacancies may occur on the Fe sublattice. This prompted us to study the effect of partial disorder on the electronic states near the Fermi level using the KKR-CPA computations. Figure 10 reports the evolution of the KKR-CPA density of states taking into account various kinds of disorders, namely $\text{Fe}_{1-x}\text{VSb}$ (vacancies on the Fe site), $\text{Fe}_{1-x}\text{VSb}_{1+x}$ (with an excess of Sb on the Fe site), $\text{Fe}_{1-x}\text{V}_{1+x}\text{Sb}$ (with an excess of V on the Fe site). One notes an unusual DOS variation versus defect concentration at the conduction band bottom both in $\text{Fe}_{1-x}\text{VSb}$ and $\text{Fe}_{1-x}\text{VSb}_{1+x}$. New states appear at the bottom of the conduction band, which are partially occupied: both the Sb excess and the Fe vacancy on the Fe lattice in FeVSb behave as electron donors. This may be understood by considering the effect of a single Sb impurity or vacancy on a Fe site. There is a much higher d -state energy for Sb impurities (s - p element) or Fe vacancies than for an Fe atom (transition element). So there is a strong repulsive perturbation in the d channel on an impurity site which expels the d states of this site from the valence band up into the lower part of the conduction band. A total of 10 filled d states is thus transferred from the valence band to the conduction band. Since 5 valence electrons are gained with the extra Sb atom and 8 valence electrons lost with the removed Fe atom, this gives a total of 7 electrons in the conduction band for each Sb impurity on the Fe site (or 2 electrons for Fe vacancies). The KKR-CPA calculations agree well with these numbers and shows that E_F is indeed located in the bottom of the conduction band. Since these KKR-CPA calculations do take into account a finite concentration of Sb impurities (or Fe vacancies) on the Fe sites they also show a significant shrinking of the perfect crystal gap. This may account for the experimental strongly doped n -type behavior of FeVSb below 650 K. From the above analysis one may also expect an unusual electronic structure in the substituted FeVSb systems if the same native crystal defects occur.

IV. DOPED FeVSb

A. Electronic structure of substituted FeVSb phases

We have investigated both n doping with cobalt and p doping with titanium and zirconium. As the site preference for the substituted atom seems to be crucial in such analysis, we first considered this point using the total energy KKR-CPA results. Indeed, computations showed (Fig. 11) that Co prefers the Fe site while both Ti and Zr should enter the V site, which supports simple expectations based on proximity in the periodic table (even at a rather high concentration). Figure 12 shows the evolution of the density of states in $\text{Fe}_{1-x}\text{Co}_x\text{VSb}$, $\text{FeV}_{1-x}\text{Ti}_x\text{Sb}$ and $\text{FeV}_{1-x}\text{Zr}_x\text{Sb}$ with $x=0.05$, 0.10, and 0.15 accounting for the chemical disorder exclusively on one site (without additional defects). The replace-

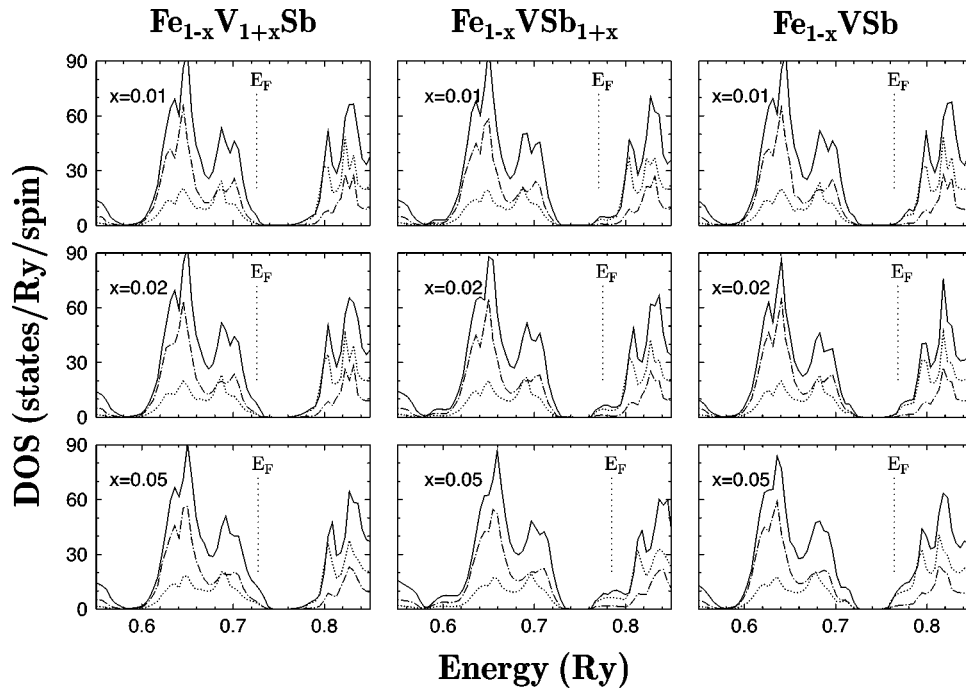


FIG. 10. KKR-CPA DOS variation versus defect size in FeVSb (see the text). $\text{Fe}_{1-x}\text{V}_{1+x}\text{Sb}$, $\text{Fe}_{1-x}\text{VSb}_{1+x}$, and $\text{Fe}_{1-x}\text{VSb}$ correspond to an excess of V, an excess of Sb, and a vacancy on the Fe sublattice, respectively. Total, Fe, and V DOS are shown by full, dot-dashed, and dotted lines, respectively.

ment of Fe by Co in $\text{Fe}_{1-x}\text{Co}_x\text{VSb}$ indeed shifts the Fermi level into the conduction states due to an increased number of electrons in the system, since d states on the dilute Co impurity on the Fe site practically do not modify the electronic structure near the gap. In the same way, the KKR-CPA computations for the Ti-doped and Zr-doped FeVSb samples show that the density of states of both impurities near the gap does not affect the electronic structure of the host leading to the Fermi level in the valence band. However, we note some differences, i.e. the Ti-DOS (mostly of d symmetry) just below the gap has a variation markedly stronger than that of the Zr-DOS, which may have some consequences on the trans-

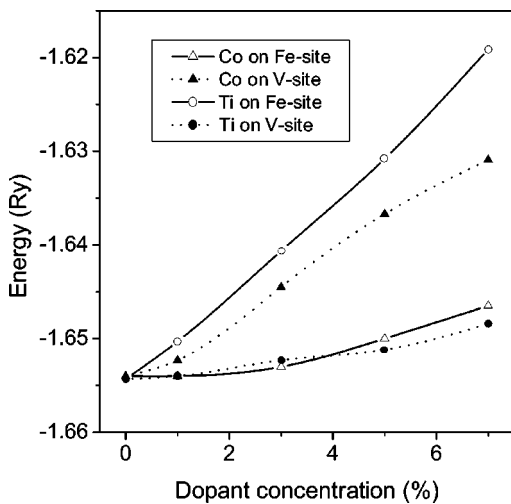


FIG. 11. Total energy of $\text{Fe}_{1-x}\text{M}_x\text{VSb}$, and $\text{FeV}_{1-x}\text{M}_x\text{Sb}$ with $M=\text{Co}, \text{Ti}$ with respect to constituent atoms.

port behavior. This simple picture may be complicated by the presence of native defects just like in the pure FeVSb case. For instance, in $\text{FeV}_{1-x}\text{Zr}_x\text{Sb}$ KKR-CPA computations accounting for an extra disorder between Fe and Sb according to the indications of the EPMA observations (Table II) lead to the results given in Fig. 13. These show that the Zr addition (holes) first compensates the native defects (electrons), and in order to observe p doping one has to add more Zr.

B. Experimental results for n doping with Co

The resistivity curves of the undoped FeVSb sample and the sample doped with 0.5% Co are similar (Fig. 14). The curve of the doped sample increases with temperature until about 750 K and, after, it decreases as for semiconductors (intrinsic regime). The Seebeck coefficient is higher than that of FeVSb (Fig. 15). The resistivity of the sample containing 2% Co is the lowest and is metallic-like in all the investigated temperature range. This is in agreement with the lower value of the Seebeck coefficient and the higher carrier concentration (Table IV). As noted above, the high Seebeck coefficient found in the 0.5% Co-doped FeVSb might be related to the strongly increasing DOS at the conduction band edge, which corresponds to an increased effective masses of electrons at E_F . With further Co substitution the density of states increases in a systematic way and the semiconducting-like behavior is lost.

C. Experimental results for p doping with Ti and Zr

Figure 16 illustrates the effect of the Ti substitution on temperature dependent resistivity curves in $\text{FeV}_{1-x}\text{Ti}_x\text{Sb}$. At

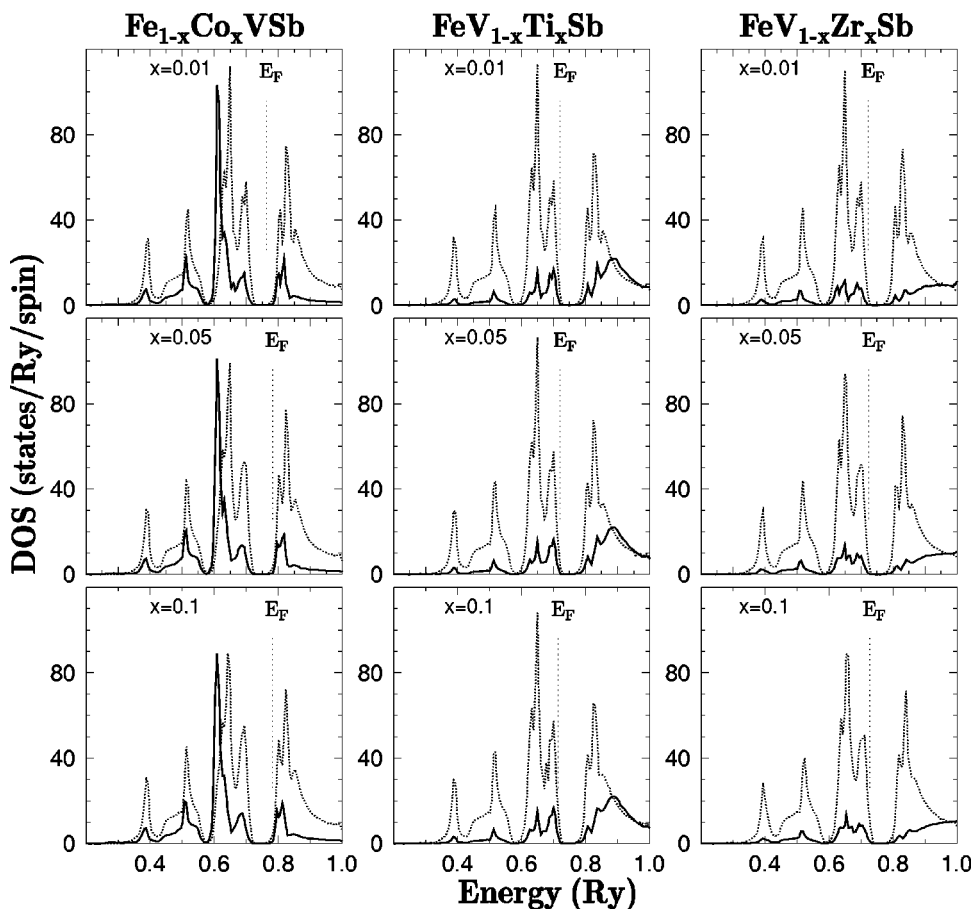


FIG. 12. KKR-CPA DOS in substituted FeVSb phases. Dotted and thick full lines represent the total and impurity (Co, Ti and Zr) DOS (in states/Ry/spin/atom), respectively.

high temperature, they tend to a common value near $20 \mu\Omega \text{ m}$, confirming the transition toward the intrinsic behavior of FeVSb. However, at a low temperature range, the resistivities are different and they range between 8 and $298 \mu\Omega \text{ m}$. Except for the sample doped with 15% titanium, the resistivity curves tend to become independent of the tem-

perature when the Ti concentration increases. The resistivity appears to be controlled by the mobility, limited by impurity disorder. In the case of $\text{FeV}_{0.85}\text{Ti}_{0.15}\text{Sb}$, a different behavior is observed. The resistivity decreases with temperature as $T^{-3/2}$ and a reduction of the carrier concentration is also observed. This semiconducting behavior is not understood yet.

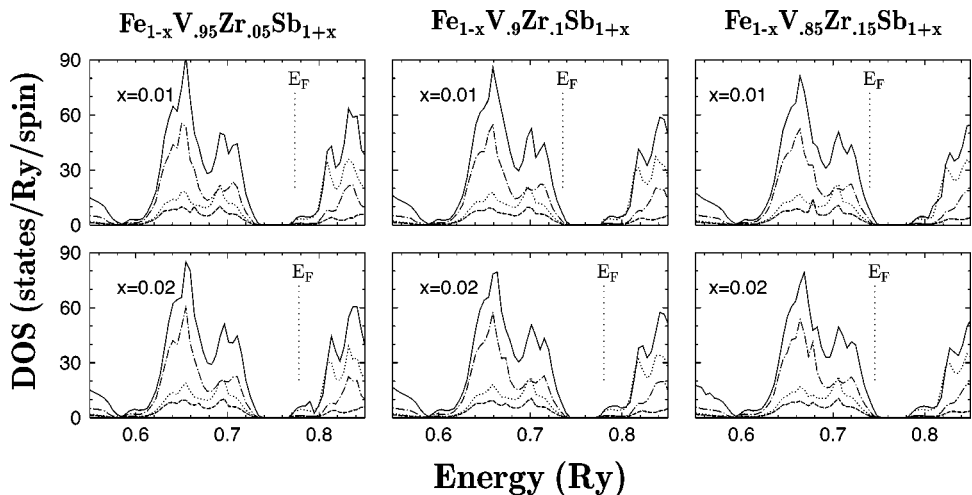


FIG. 13. KKR-CPA DOS in $\text{Fe}_{1-x}(\text{V-Zr})\text{Sb}_{1+x}$ (with 0.05, 0.1, and 0.15 Zr contents) versus Fe/Sb defects (see the text). Total, Fe, V, and Zr-DOS are shown by full, dot-dashed, dotted, and dashed lines, respectively.

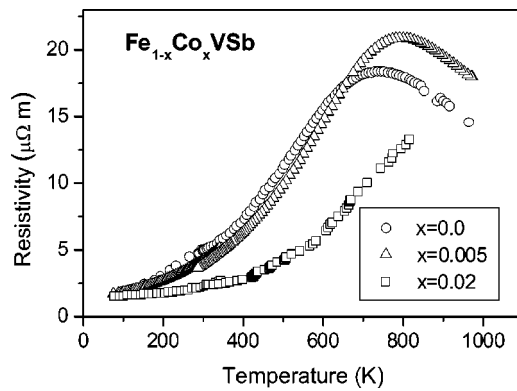


FIG. 14. Temperature dependence of the electrical resistivity in $\text{Fe}_{1-x}\text{Co}_x\text{VSb}$.

All Ti-containing samples show a positive Seebeck coefficient at room temperature. Within the $\text{FeV}_{1-x}\text{Ti}_x\text{Sb}$ series of compounds the largest thermopower value was reached in $\text{FeV}_{0.95}\text{Ti}_{0.05}\text{Sb}$ (+180 $\mu\text{V}/\text{K}$) and then it decreases systematically when the Ti content increases. Figure 15 shows $S(T)$ curves in $\text{FeV}_{1-x}\text{Ti}_x\text{Sb}$. A flat maximum of $S(T)$ can be observed in the 500–600 K temperature range depending on the Ti content. Note that no peculiar thermopower behavior was detected in the $x=0.15$ sample, in spite of a resistivity variation qualitatively different from other Ti contents. This might be due to some sort of impurity ordering, but the structural studies did not show anything. A strong decrease of the thermopower for $T > 600$ K in $\text{FeV}_{0.95}\text{Ti}_{0.05}\text{Sb}$ is due to a rapid compensation of holes (dominating at low temperatures) by thermally activated electrons when the temperature approaches the intrinsic range. In phases containing more Ti, the $S(T)$ variations are slower. Although in the thermopower measurements we obtained a high and positive S even at $x=0.05$ Ti, a change of the Seebeck coefficient sign in $\text{FeV}_{1-x}\text{Ti}_x\text{Sb}$ (from high and negative at $x=0.05$ to high and positive in $x=0.15$) was previously observed.²⁷ From the KKR-CPA results this might indicate that the two sets of

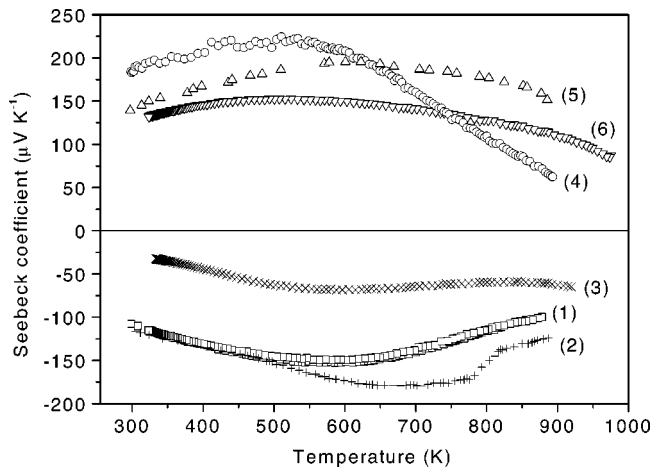


FIG. 15. Temperature dependence of the Seebeck coefficient in half-Heusler phases: (1) FeVSb ; (2) $\text{Fe}_{0.995}\text{Co}_{0.005}\text{VSb}$; (3) $\text{FeV}_{0.95}\text{Zr}_{0.05}\text{Sb}$; (4) $\text{FeV}_{0.95}\text{Ti}_{0.05}\text{VSb}$; (5) $\text{FeV}_{0.9}\text{Ti}_{0.1}\text{VSb}$; (6) $\text{FeV}_{0.85}\text{Ti}_{0.15}\text{VSb}$.

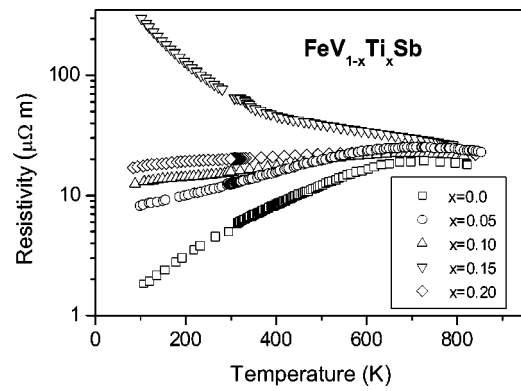


FIG. 16. Temperature dependence of the electrical resistivity in $\text{Fe}_{1-x}\text{Ti}_x\text{VSb}$.

samples contained different amounts of compensated native crystal defects.

The substitution with Zr leads to radical change of the temperature dependent resistivity curves. From Fig. 17 we see that all Zr-containing samples exhibit a semiconducting-like character of resistivity curves. The strongest $d\rho/dT$ slope was observed at $x=0.02$, while other samples exhibit ρ decreasing versus T more and more moderately as the Zr content increases. The change in the $d\rho/dT$ slope versus Zr content is accompanied by a systematic increase of the hole concentration, as found in the Hall effect measurements (Table IV). The Seebeck coefficient in $\text{FeV}_{1-x}\text{Zr}_x\text{Sb}$ changes sign from negative to positive when the Zr content increases. This can be understood if the compensation of electrons due to native defects is taken into account (Fig. 13). The $S(T)$ curves measured in $\text{FeV}_{0.98}\text{Zr}_{0.02}\text{Sb}$ indicates that the thermopower is more or less constant over the whole temperature range.

As seen in Fig. 12 and 13, the Ti-DOS being located just below the gap varies much more strongly than the Zr-DOS. Such features may also contribute to the larger Seebeck coefficient in the Ti-doped samples with respect to the Zr-doped case. Both the positive sign and the thermopower decrease with the Ti content can be attributed to the Fermi level position in the valence states and the increasing DOS at E_F found in the computations.

V. CONCLUSIONS

The resistivity and thermopower measurements in the range of temperature 80–800 K in pure and substituted

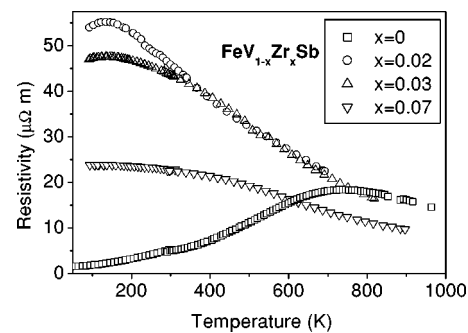


FIG. 17. Temperature dependence of the electrical resistivity in $\text{FeV}_{1-x}\text{Zr}_x\text{Sb}$.

TABLE IV. Room temperature Seebeck coefficient S and resistivity ρ in pure and substituted FeVSb half-Heusler phases.

Composition	ρ ($\mu\Omega$ m)	S ($\mu\text{V K}^{-1}$)	$n \times 10^{20}$ (cm^{-3})
FeVSb	5.1	-110	≈ 1
Fe _{0.995} Co _{0.005} VSb	4.2	-130	≈ 1
Fe _{0.98} Co _{0.02} VSb	2.3	-80	≈ 5
FeV _{0.95} Ti _{0.05} Sb	13	+180	≈ 5
FeV _{0.90} Ti _{0.10} Sb	15.5	+145	≈ 5
FeV _{0.85} Ti _{0.15} Sb	68.7	+125	≈ 2
FeV _{0.80} Ti _{0.20} Sb	20	+70	≈ 20
FeV _{0.95} Zr _{0.02} Sb	46	-20	≈ 1
FeV _{0.90} Zr _{0.03} Sb	43	+20	≈ 3
FeV _{0.85} Zr _{0.07} Sb	23	+30	≈ 4

(Co, Ti, Zr) FeVSb samples showed that their transport properties seem to originate not only from the type of doping (hole or electron) of the substituted impurities, but also from the native defects occurring in the systems. Indeed, the structural analysis showed that most investigated samples contained an excess of Sb (or vacancies on the Fe sublattice) as well as the disorder between V and Sb.^{45,46}

The resistivity in FeVSb increased with temperature in a metallic-like way, reaching a maximum near 650 K, which was identified as the transition into an intrinsic semiconducting regime. The thermopower is large and negative.

The KKR-CPA study of various types of disorder in FeVSb (nonstoichiometry, anti-site defects) revealed a remarkable effects on density of states in the vicinity of the gap, upon accounting for Sb impurity on Fe site and Fe vacancies. In such cases the simple VEC=18 rule for the semiconductivity occurrence in the half-Heusler systems, is no longer maintained. All these results together show that FeVSb as well as other VEC=18 half-Heusler compounds⁴⁷ may also exhibit metallic-like behaviors at low temperatures. On the other hand, the rather high thermopower observed in this compound allows classifying FeVSb as a “dirty” semiconductor.

In Fe_{1-x}Co_xVSb, $\rho(T)$ characteristics tended to metallic-like behavior with an increasing cobalt content. A large and negative Seebeck coefficient was detected at a small amount of Co, whereas the thermopower was much smaller in the

$x=0.02$ sample. This was also supported by the electronic structure calculations showing that the Fermi level shifts into the conduction band versus the cobalt doping without DOS shape modifications. The system becomes then more metallic. Moreover, the native n -type defects could not markedly change this effect.

In the Ti-containing samples the thermopower was positive and large, as expected in systems doped with p -type elements, but the change of the $d\rho(T)/dT$ slope observed in FeV_{1-x}Ti_xSb for $x=0.15$ appeared anomalous and was not supported by the KKR-CPA DOS variation.

In FeV_{1-x}Zr_xSb the Seebeck coefficient was much smaller than in isoelectronic FeV_{1-x}Ti_xSb and changed sign from negative ($x=0.02, S=-20\mu\text{V/K}$) to positive ($x=0.03, S=+40\mu\text{V/K}$). In view of the electronic structure KKR-CPA computations such a phenomenon seems to be possible when extra crystal defects, as detected by the EPMA analysis, are taken into account in the calculations. Fe vacancies or an Sb excess on the Fe-site introduce extra electrons, which may not be compensated for low Zr doping.

In summary, this theoretical KKR-CPA study shows that crystal imperfections may have a crucial role in electron transport behaviors of the pure FeVSb and Co-, Ti-, and Zr-substituted phases. Experimental data cannot be interpreted coherently from perfect crystal calculations. This conclusion also seems to be relevant to other half-Heusler systems with valence electrons close to 18, when various crystal defects appear.

In the present paper we concentrate on the electronic properties of pure and doped FeVSb. To assess these materials value as thermoelectrics, their thermal conductivities λ have to be measured and the so-called factor of merit $Z = S^2/\rho\lambda$ must be evaluated. Some preliminary measurements have been performed.⁴⁸ The highest values have been obtained at $T \approx 600$ K for FeV_{0.95}Ti_{0.05}Sb ($Z=0.45$) and FeCo_{0.995}Ti_{0.005}Sb ($Z=0.34$). These values are not bad, but they are still insufficient for high performance thermoelectrics.

ACKNOWLEDGMENT

We are indebted to Professor E. McRae (LCSM UHP, Vandoeuvre-les-Nancy) for his critical reading of the manuscript.

*Also at Faculty of Physics and Nuclear Techniques, AGH University of Science and Technology, Al. Mickiewicza 30, 30-059 Cracow, Poland.

¹R. A. de Groot, F. M. Mueller, P. G. van Engen, and K. H. J. Buschow, Phys. Rev. Lett. **50**, 2024 (1983).

²P. J. Webster and K. R. A. Ziebeck, in *Magnetic Properties of Metals and Alloys*, Landolt-Bornstein New Series, edited by O. Madelung (Springer-Verlag, Berlin, 1988), Vol. III/19c, pp. 75–184.

³J. Pierre, R. V. Skolozdra, J. Tobola, S. Kaprzyk, C. Hordequin,

M. A. Kouacou, I. Karla, R. Currat, and E. Lelievre-Berna, J. Alloys Compd. **262–263**, 101 (1997).

⁴J. Tobola, S. Kaprzyk, R. V. Skolozdra, and M. A. Kouacou, J. Phys.: Condens. Matter **10**, 1013 (1998).

⁵J. Tobola and J. Pierre, J. Alloys Compd. **296**, 243 (2000).

⁶F. G. Aliev, F. G. Brandt, V. V. Moshchalkov, V. Kozyrkov, R. V. Skolozdra, and A. I. Belogorov, Z. Phys. B: Condens. Matter **75**, 167 (1989).

⁷F. G. Aliev, V. Kozyrkov, V. V. Moshchalkov, R. V. Skolozdra, and K. Durczewski, Z. Phys. B: Condens. Matter **80**, 353

- (1990).
- ⁸S. Ogut and K. M. Rabe, Phys. Rev. B **51**, 10 443 (1995).
- ⁹J. Tobola, J. Pierre, S. Kaprzyk, R. V. Skolozdra, and M. A. Kouacou, J. Magn. Magn. Mater. **159**, 192 (1996).
- ¹⁰S. Ishida, I. Masaki, S. Fujii, and S. Asano, Physica B **42**, 363 (1997).
- ¹¹A. Slebarski, A. Jeziarski, A. Zygmunt, S. Mahl, and M. Neumann, Phys. Rev. B **57**, 9544 (1998).
- ¹²M. Springborg, B. Sang, and M. L. Persson, J. Phys.: Condens. Matter **11**, 1669 (1999).
- ¹³P. Larson, S. D. Mahanti, S. Sportouch, and M. G. Kanatzidis, Phys. Rev. B **59**, 15 660 (1999).
- ¹⁴I. Galanakis, P. H. Dederichs, and N. Papanikolaou, Phys. Rev. B **66**, 134428 (2002).
- ¹⁵J. Tobola, P. Pecheur, H. Scherrer, J. Pierre, and S. Kaprzyk, *Proceedings of the 19th International Conference on Thermoelectrics* (Babrow Press, Cardiff, Wales, 2001).
- ¹⁶L. Jodin, J. Tobola, P. Pecheur, and H. Scherrer, *Proceedings of the 20th International Conference on Thermoelectrics* (IEEE, Piscataway, NJ, 2001), pp. 240–246.
- ¹⁷C. B. H. Evers, C. R. Richter, K. Hajtjes, and W. Jeitschko, J. Alloys Compd. **252**, 93 (1997).
- ¹⁸H. Hohl, A. P. Ramirez, C. Goldman, G. Ernst, B. Wolfing, and E. Bucher, J. Phys.: Condens. Matter **10**, 7843 (1998).
- ¹⁹C. S. Lue, Y. Oner, D. G. Naugle, and J. H. Ross, IEEE Trans. Magn. **37**, 2138 (2001).
- ²⁰H. Hohl, A. P. Ramirez, C. Goldman, G. Ernst, B. Wolfing, and E. Bucher, J. Phys.: Condens. Matter **11**, 1697 (1999).
- ²¹C. Uher, J. Yang, S. Hu, D. T. Morelli, and G. P. Meisner, Phys. Rev. B **59**, 8615 (1999).
- ²²Y. Xia, S. Bhattacharya, V. Ponnambalam, A. L. Pope, S. J. Poon, and T. M. Tritt, J. Appl. Phys. **88**, 1952 (2000).
- ²³Y. Xia, V. Ponnambalam, S. Bhattacharya, A. L. Pope, S. J. Poon, and T. M. Tritt, J. Phys.: Condens. Matter **13**, 77 (2001).
- ²⁴S. J. Poon, Semicond. Semimetals **70**, 37 (2001), and references therein.
- ²⁵Q. Shen, L. Chen, T. Goto, T. Hirai, J. Yang, G. P. Meisner, and C. Uher, Appl. Phys. Lett. **79**, 4165 (2001).
- ²⁶K. Kaczmarek, J. Pierre, J. Tobola, and R. V. Skolozdra, J. Magn. Magn. Mater. **187**, 210 (1998).
- ²⁷D. Young, P. Khalifah, R. J. Cava, and A. P. Ramirez, J. Appl. Phys. **87**, 317 (2000).
- ²⁸J. Pierre and I. Karla, J. Magn. Magn. Mater. **217**, 74 (2000).
- ²⁹J. Tobola, L. Jodin, P. Pecheur, H. Scherrer, G. Venturini, B. Malaman, and S. Kaprzyk, Phys. Rev. B **64**, 155103 (2001).
- ³⁰J. Tobola, L. Jodin, P. Pecheur, and G. Venturini, J. Alloys Compd. **383**, 328 (2004).
- ³¹P. Villars and L. D. Calvert, in *Pearson's Handbook on Intermetallic Phases* (ASM International, Metals Park, OH, 1997).
- ³²B. Malaman (private communication).
- ³³J. Rodriguez-Carvajal, Physica B **192**, 55 (1993).
- ³⁴U. von Barth and L. Hedin, J. Phys. C **5**, 1629 (1972).
- ³⁵S. Kaprzyk and A. Bansil, Phys. Rev. B **42**, 7358 (1990).
- ³⁶A. Bansil, S. Kaprzyk, and J. Tobola, in *Applications of Multiple Scattering Theory in Material Science*, edited by W. H. Butler, P. H. Dederichs, A. Gonis, and R. Weaver, MRS Symposia Proceedings, No. 253 (MRS, Pittsburgh, 1992), p. 505.
- ³⁷A. Bansil and S. Kaprzyk, Phys. Rev. B **43**, 10 335 (1991).
- ³⁸S. Kaprzyk, Acta Phys. Pol. A **91**, 135 (1997).
- ³⁹A. Bansil, S. Kaprzyk, P. E. Mijnarends, and J. Tobola, Phys. Rev. B **60**, 13 396 (1999).
- ⁴⁰H. van Leuken and R. A. de Groot, Phys. Rev. Lett. **74**, 1171 (1995).
- ⁴¹B. R. K. Nanda and I. Dasgupta, J. Phys.: Condens. Matter **15**, 7307 (2003).
- ⁴²D. Jung, H. J. Koo, and M. H. Whangbo, J. Mol. Struct.: THEOCHEM **527**, 113 (2000).
- ⁴³L. P. van der Pauw, Philips J. Res. **13**, 9 (1958).
- ⁴⁴C. Wood, D. Zoltan, and G. Stapfer, Rev. Sci. Instrum. **56**, 719 (1985).
- ⁴⁵P. Larson, S. D. Mahanti, and M. G. Kanatzidis, Phys. Rev. B **62**, 12 754 (2000).
- ⁴⁶R. Weht and W. E. Pickett, Phys. Rev. B **58**, 6855 (1998).
- ⁴⁷L. Degiorgi, A. V. Sologubenko, H. R. Ott, F. Drymiotis, and Z. Fisk, Phys. Rev. B **65**, 041101 (2001).
- ⁴⁸L. Jodin, Thesis, Institut National Polytechnique de Lorraine, Nancy, France, 2002.